Ancient atmospheric noble gases preserved in post-impact hydrothermal minerals of the 200 Ma-old Rochechouart impact structure, France

Guillaume Avice, M.A. Kendrick, A. Richard, L. Ferrière

Earth and Planetary Science Letters 620 (2023) 118351

Contents lists available at ScienceDirect

Earth and Planetary Science Letters

journal homepage: www.elsevier.com/locate/epsl

Ancient atmospheric noble gases preserved in post-impact hydrothermal minerals of the 200 Ma-old Rochechouart impact structure, France

G. Avice [a,*], M.A. Kendrick [b], A. Richard [c], L. Ferrière [d]

[a] Université Paris Cité, Institut de physique du globe de Paris, CNRS, F-75005 Paris, France
[b] School of Earth and Environmental Sciences, The University of Queensland, Brisbane, Queensland 4072, Australia
[c] Université de Lorraine, CNRS, GeoRessources, F-54506, Vandoeuvre-lès-Nancy, France
[d] Natural History Museum Vienna, Burgring 7, A-1010 Vienna, Austria

ARTICLE INFO

Article history:
Received 6 February 2023
Received in revised form 3 August 2023
Accepted 6 August 2023
Available online xxxx
Editor: R. Dasgupta

Keywords:
geochemistry
noble gases
impact crater
hydrothermal quartz
paleo-atmosphere
fluid inclusion

ABSTRACT

The evolution of Earth's atmosphere over billions of years provides important constraints on the geological history of our planet. However, major challenges in studying this have been finding samples in which ancient atmospheric signals are reliably preserved and precisely determining the age of the trapped atmosphere. Hydrothermal minerals can preserve fluid inclusions that formed from air-saturated waters. However, the use of hydrothermal minerals as paleo-atmospheric proxies is often limited by contamination by deeply-sourced crustal gases (e.g., radiogenic noble gases) and the difficulty of providing precise age constraints on the crystallization of the hydrothermal minerals.

In this study, we tested the hypothesis that meteorite impact craters could provide an untapped archive of atmospheric evolution by investigating noble gases (Ne, Ar, Kr and Xe) contained in fluid inclusions within post-impact hydrothermal minerals from the Rochechouart impact structure (France). Impact craters can be dated using a variety of methods and because meteorite impacts cause localized fracturing of country rocks and the development of minor thermal anomalies, they are often associated with short-lived (up to a few Ma, depending on the size of the crater) and shallow hydrothermal systems dominated by surface-derived hydrothermal fluids.

We found that the elemental ratios of noble gases in quartz from Rochechouart are close to the elemental ratios of modern Air. Furthermore, most noble gas isotope ratios are close to modern atmosphere, except for rare deviations caused by radiogenic ingrowth, nucleogenic effects and/or minor mass fractionation. After a minor correction for post-entrapment decay of ^{40}K, an upper limit for the $^{40}Ar/^{36}Ar$ ratio of the ~200 Ma atmospheric component trapped in Rochechouart quartz is determined as 292.7 ± 3.6 (2σ s.d.), which is significantly lower than the modern value of 298.6 ± 0.3. A Mesozoic $^{40}Ar/^{36}Ar$ ratio lower than 292.7 ± 3.6 is in line with the existing paleo-atmospheric dataset and existing models of the temporal evolution of the atmospheric $^{40}Ar/^{36}Ar$ ratio and conclusively proves the preservation of an ancient atmospheric component in rocks from Rochechouart. Given that meteorite impacts have occurred throughout the entire Earth's history they might collectively provide a unique, yet unexplored, repository of the atmospheric evolution. The same approach might also be applicable to investigating the atmospheric evolution of other terrestrial planets.

1. Introduction

Earth's modern atmosphere is unique in our solar system and differs greatly from the one that surrounded the Archean or Proterozoic Earth (see the review by Catling and Zahnle, 2020). The evolution of Earth's atmosphere results from a complex interplay between biological activity, chemical drawdown of CO_2 in liquid water, volcanism, and external processes such as atmospheric escape and volatile delivery by impacts that were most important on the early Earth (Catling and Kasting, 2017; Ehlmann et al., 2016). Noble gases represent about 1% of the Earth's modern atmosphere. Studying the elemental abundances and isotope composition of

* Corresponding author.
E-mail address: avice@ipgp.fr (G. Avice).

https://doi.org/10.1016/j.epsl.2023.118351

noble gases provides constraints on models for the origin and evolution of abiogenic non-reactive components in planetary atmospheres (Burnard, 2013; Marty, 2020; Ozima and Podosek, 2002). Samples of paleo-atmosphere preserved in terrestrial materials can provide additional constraints on processes that have shaped our atmosphere, including changes in the parameters powering atmospheric escape (Avice et al., 2018) and the evolution of Earth's geodynamics (Pujol et al., 2013; Stuart et al., 2016).

A critical step to studying the paleo-atmosphere is finding additional reliable proxies for the composition of the ancient atmosphere. Paleo-atmospheric proxies must satisfy two main criteria: i) they need to trap ancient atmosphere and faithfully preserve its composition over geological time; ii) the age of the trapped atmospheric signal should be known. Access to ancient atmospheric gases contained in minerals is limited by geological reworking and/or alteration of materials by erosion, tectonics, and metamorphism. However, a few studies have demonstrated that paleo-atmospheric noble gases can be preserved in ancient hydrothermal minerals (*e.g.*, Almayrac et al., 2021; Ardoin et al., 2022; Avice et al., 2017, 2018; Broadley et al., 2022; Marty et al., 2013; Pujol et al., 2013), although isolating the ancient atmospheric signal and verifying its age can be challenging (Avice et al., 2017; Turner, 1988). In this context, hydrothermal minerals formed by the precipitation of solids from fluids circulating through fractured rocks within meteorite impact craters could be a promising new paleo-atmospheric proxies. Firstly, meteorite impact craters with a wide range of ages are known (e.g., Osinski et al., 2022; Schmieder and Kring, 2020), although it should be noted that the age of many of them is still rather poorly constrained (see e.g., Jourdan et al., 2012; Schmieder and Kring, 2020). However, thanks to the advance of modern mass spectrometry, much more precise isotopic ages can be obtained these days, and more and more impact craters ages are being refined (e.g., Holm-Alwmark et al., 2021). This offers the opportunity to sample atmospheric gases of various ages and to follow the evolution of the atmosphere from the Paleoproterozoic to Modern geological time. Secondly, fracturing and thermal anomalies generated by impacts often lead to the development of post-impact hydrothermal systems that are relatively short-lived and shallow, meaning they are likely to be dominated by air-saturated waters (Naumov, 2002). The mineral paragenesis of post-impact hydrothermal systems typically follows a retrograde sequence of alteration and the presence of hydrothermal quartz, in some cases containing fluid inclusions, is repeatedly mentioned in the literature. Analyses of fluid inclusions in those hydrothermal quartz often identify a fluid with low salinity (Naumov, 2002 and references therein). Importantly, due to the relatively shallow nature of the impact craters, fluids trapped in those fluid inclusions could preserve an atmospheric signature. Lastly, numerical simulations and age determination studies demonstrated that impact-generated hydrothermal systems should likely be short lived, lasting at maximum a few million years in the case of the largest impact craters (Abramov, 2004; Ames et al., 1998). For all these reasons, post-impact hydrothermal lithologies could provide "snapshots" of the composition of the ancient atmosphere.

The goal of the present study is to test the potential of post-impact hydrothermal minerals as paleo-atmospheric proxies. We measured noble gases trapped in fluid inclusions contained in post-impact hydrothermal minerals of the 200 Ma-old Rochechouart impact structure (see Sapers et al., 2014 and references therein). We demonstrate that gases from the 200 Ma-old atmosphere are present within these samples and that the paleo-atmospheric record is well preserved.

2. Material and methods

2.1. Geological setting

The Rochechouart impact structure is located at the N-W border of the Massif Central in France. No specific topographic feature of the impact structure is visible at the surface due to erosion. An impact origin was first proposed based on the occurrence of quartz grains with planar deformation features (PDFs) and then confirmed with the observation of shatter cones (Kraut, 1969; Kraut and French, 1971). An age of 206.92±0.32 Ma for the impact has been recently estimated based on Ar-Ar dating of potassium feldspars from a sample of the Babaudus impact melt rock (Cohen et al., 2017). Target lithologies containing hydrothermal quartz related to the impact include basement granite, gneiss, and other metamorphosed rocks (Turpin et al., 1990). The geology of the Rochechouart impact site is reviewed in detail by Sapers et al. (2014).

Post-impact hydrothermal circulation at the Rochechouart impact site is preserved in a sequence of hydrothermal minerals (Kraut and French, 1971) broadly similar to the parageneses reported for other post-impact hydrothermal settings (Naumov, 2002). Breccias cemented by hydrothermal quartz are common (Sapers et al., 2014), and are especially well developed in the Champagnac quarry, the main sampling area for the present study. Samples from the impact-generated hydrothermal system of the Rochechouart impact structure represent a perfect opportunity to test the potential of post-impact hydrothermal minerals as paleo-atmospheric proxies since i) except for an increase of the atmospheric $^{40}Ar/^{36}Ar$ ratio (*e.g.*, Stuart et al., 2016) the composition of noble gases in the Earth's atmosphere is expected to have been constant for the last 200 Myr (Avice and Marty, 2020); ii) the Rochechouart area has not been disturbed by post-impact heating events (Schmieder et al., 2010) and refs. therein or by any significant tectonic movements (Bischoff and Oskierski, 1987) meaning that if present, ~200 Ma paleo-atmospheric signatures could be well preserved in the rocks there.

2.2. Samples

All samples analyzed in this study are from the impactite collection of the Natural History Museum Vienna (Austria) and were collected by P. Chèvremont during research activities in the Rochechouart area including for geological mapping (Chèvremont et al., 1996). All the samples except one come from the Champagnac quarry (45°51′19″N, 0°49′56″E) where the post-impact hydrothermal minerals are well exposed. Most samples consist in quartz veins cross-cutting basement rocks (Fig. 1). One sample (ROC-AGATA4) is an agate nodule made of chalcedony, a complex intergrowth of small quartz and moganite crystals, found within a vesicular, clast-poor, impact melt rock (so-called "Babaudus impact melt"; See Sapers et al., 2014). It was found as a boulder by an inhabitant in his garden at the hamlet of Valette (village of Pressignac; ~45°48′48″N, 0°46′32″E). This nodule likely formed by hydrothermal vesicle filling, relatively soon after the impact event, as in the case of similar agate nodules found at e.g., the Ilyinets impact structure in Ukraine (Gurov et al., 1998) and at the Sääksjärvi impact structure in Finland (Kinnunen and Lindqvist, 1998). Sample ROC20-2 consists of a quartz-filled cavity with carbonate crystals in the center.

2.3. Methods

After preliminary observations, samples were cut with a diamond saw. One section was dedicated to the preparation of thick sections for petrographic observations. The other section was used to prepare pure mineral fractions by manual crushing, sieving, and

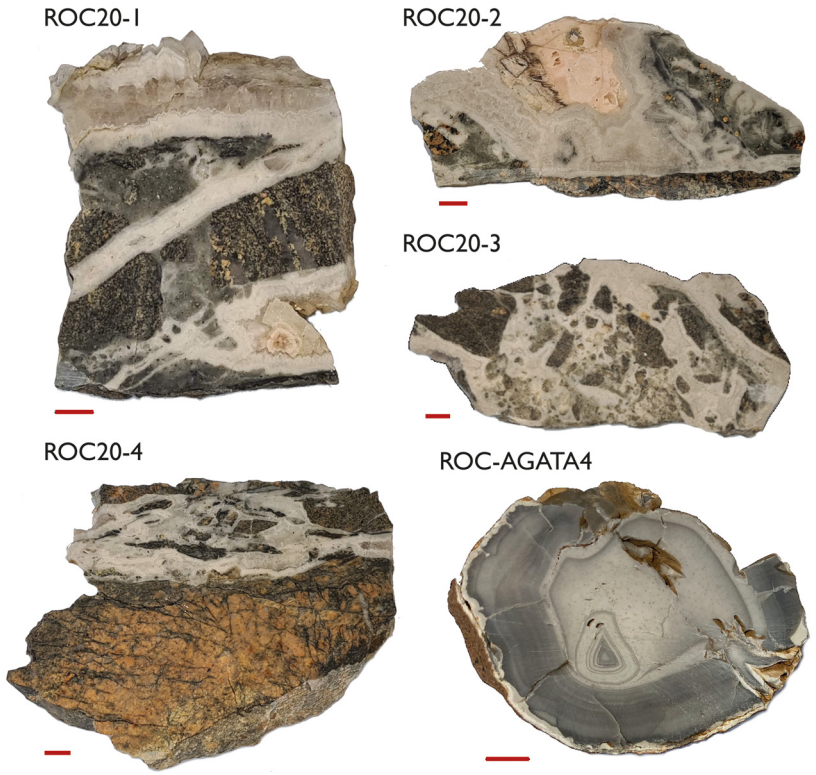

Fig. 1. Macrophotographs of the samples analyzed in this study. Quartz crystals appear in white. ROC20-1: quartz crystals with visible growth pattern are observed at the top. ROC20-2: the pink-colored crystals at the center correspond to carbonate. ROC-AGATA4 is an agate sample showing concentric zoning of silica. Scale bars correspond to 1 cm.

by hand picking of pure quartz grains with size ranging from 1 to 5 mm under the binocular microscope. All grains were washed ultrasonically in acetone and dried under an infrared lamp. One or two aliquots of each sample (~ 0.4-1.0 g) were dedicated to noble gas analyses of non-irradiated samples at the Université Paris Cité (ROC20-1, ROC20-2, ROC20-2bis, ROC20-2carb., ROC20-3, ROC20-4, and ROC-AGATA4). Separate aliquots of each sample were used for Ar-Ar measurements at the University of Queensland and are identified with "Ar-Ar" in the following text and figures (ROC20-1 Ar-Ar, ROC20-2 Ar-Ar, ROC20-3 Ar-Ar, ROC20-4 Ar-Ar, and ROC-AGATA4 Ar-Ar).

2.4. Petrology and fluid inclusion characterization

Five polished thin sections (25 µm in thickness) and five doubly polished thicker sections (150 µm) were prepared and studied with an Olympus BX51 optical microscope and a Keyence VHX - 1000 digital optical microscope at the GeoRessources laboratory (Nancy, France) (Fig. 2). Petrographic analysis of the veins was carried out on thin sections according to Bons et al. (2012) and Passchier and Trouw (2005). Petrographic analysis of fluid inclusions was carried out at room temperature on thick sections according to Van den Kerkhof and Hein (2001) and Wilkinson (2001).

Sample ROC-AGATA4 shows typical cryptocristalline texture of chalcedony with disseminated iron oxide inclusions and no optically visible fluid inclusions (Fig. 2a). In ROC20-1 and ROC20-4, quartz veins crosscut altered (chloritized) basement rocks and display typical syntaxial texture (Fig. 2a, b). In sample ROC20-2 a massive quartz vein crosscuts altered basement rocks and shows a late carbonate infilling (Fig. 2c). Sample ROC20-3 is a quartz-filled breccia within altered basement rocks (Fig. 2d). In all samples, quartz shows variable textures: saccharoid, comb-like, euhedral blocky, and blocky elongated. Quartz crystals show cloudy cores (i.e., fluid inclusion-rich) and growth bands as underlined by variable fluid inclusion abundances (cloudy versus more translucent fluid inclusions-poor domains), or more patchy distribution of fluid inclusion-rich and fluid inclusion-poor domains (Fig. 2e, f).

Optically visible fluid inclusions are typically 1-15 microns in size and show irregular shape. Fluid inclusion assemblages are either primary (i.e., along quartz growth bands, or intragranular clusters) or pseudosecondary (i.e., intragranular fluid inclusion planes) and therefore they have trapped fluids that circulated within the fractures during quartz±carbonate growth. Three types of fluid inclusion assemblages have been identified within quartz and carbonate, showing variable apparent volumetric fraction of the vapor phase relative to the entire inclusion (φ_{vap}). Type 1 assemblages are composed of coexisting one-phase inclusions (liquid) and two-phase inclusions (liquid + vapor) with φ_{vap} = 5-10% and a vapor bubble sometimes moving) (Fig. 2g). Type 2 assemblages are composed of coexisting one-phase inclusions (liquid), two-phase inclusions (liquid + vapor) with φ_{vap} = 5-10%, two-phase inclusions (liquid + vapor) with φ_{vap} = 10-99%, and one-phase inclusions (vapor) (Fig. 2h). Type 3 assemblages are composed of coexisting one-phase inclusions (vapor/φ_{vap} = 100%) only (Fig. 2i). Type 1 assemblages are typical of low temperature and pressure homogeneous trapping of a liquid fluid with metastable one-phase inclusions (liquid) having failed to nucleate a vapor bubble upon cooling to room temperature. Type 2 assemblages are typical high temperature and low-pressure boiling assemblages typical of near surface epithermal hydrothermal systems. Type 3 assemblages are also diagnostic of near surface epithermal hydrothermal systems where fluids undergo boiling. Altogether, petrographic observations of hydrothermal quartz, carbonate, and fluid inclusions indicate near-surface conditions of high-temperature fluids undergoing boiling. This is compatible with the expected conditions prevailing around impact craters during cooling of the country rocks after the impact (*e.g.*, Naumov, 2002).

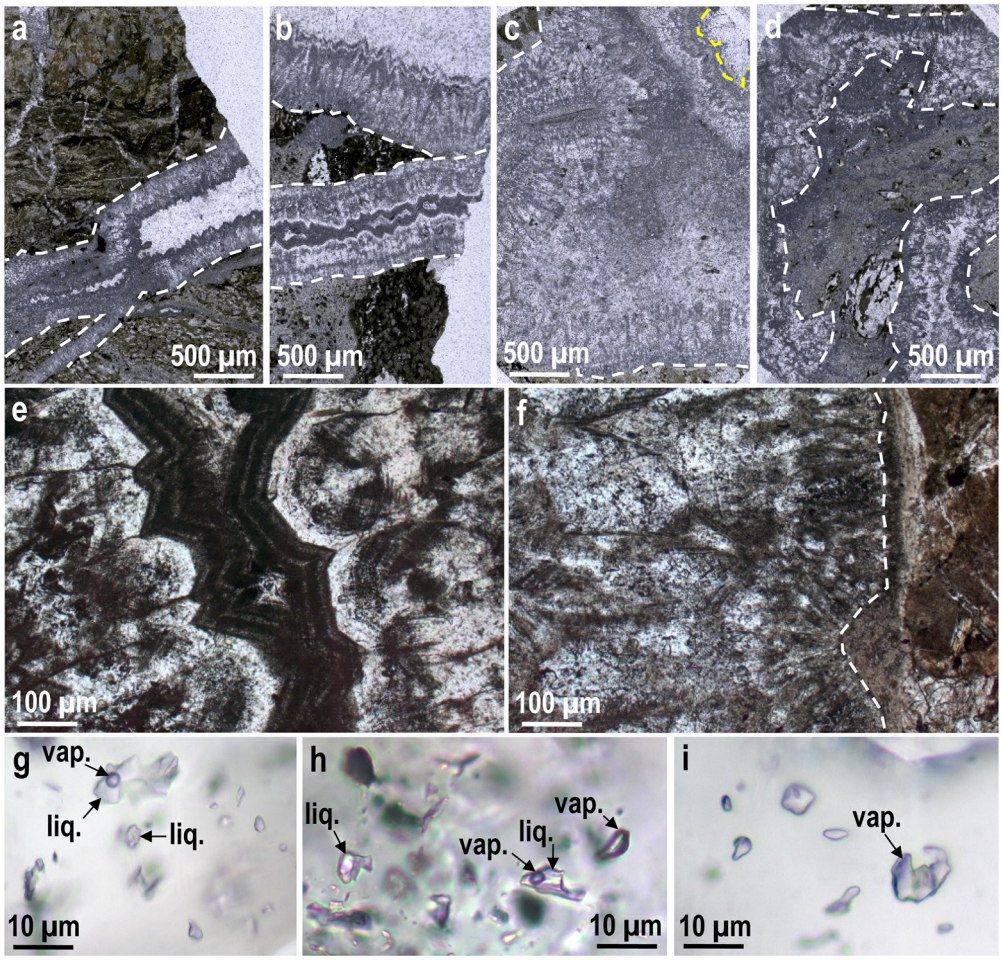

Fig. 2. Summary of petrographic observations of hydrothermal quartz ± carbonate veins and breccias and their fluid inclusions analyzed in this study (in plane-polarized light). Vein selvages are underlined by dashed white lines. a) Sample ROC20-4. Syntaxial quartz vein. b) Sample ROC20-1. Two crosscutting syntaxial quartz veins. c) Sample ROC20-2. Complex massive quartz-carbonate vein. Carbonate postdates quartz (carbonate is surrounded by a dashed yellow line). d) Sample ROC20-3. Quartz-filled breccia. e) Detailed view of sample ROC20-1 showing cloudy (i.e., fluid inclusion-rich) and more translucent (i.e., fluid inclusion-poor) quartz domains underlining growth bands. f) Detailed view of sample ROC20-2 showing complex arrays of cloudy and more translucent quartz domains. g) Type 1 fluid inclusion assemblage showing one-phase inclusions (liquid) and two-phase inclusions (liquid + vapor). h) Type 2 fluid inclusion assemblage showing one-phase inclusions (liquid), two-phase inclusions (liquid + vapor), and one-phase inclusions (vapor). i) Type 3 fluid inclusion assemblage showing one-phase inclusions (vapor). liq.: liquid phase; vap.: vapor phase.

2.5. Noble gas analyses of non-irradiated samples

Noble gases were extracted from fluid inclusions of non-irradiated samples by step-crushing in ultra-high vacuum conditions. This approach used in previous studies allows to progressively release gases trapped in fluid inclusions (see above) and to reveal atmospheric signals (*e.g.*, Avice et al., 2018). The crusher consisted of a bottom-closed stainless-steel tube containing the sample and an iron ball. Crushing proceeded by manually lifting and projecting the ball against the sample grains with a hand-magnet placed outside the vacuum. During crushing, a pressure gauge monitored the pressure of the extracted gases collected in the vacuum line. After extraction, the noble gases were purified using three getter pumps to sequentially remove active gases. Gas was first exposed to a getter of St707 pellets (SAES) held at 600 °C for 5 mins and then cooled for 10 mins with the getter furnace off. The following two getters contained titanium sponge and were held at 650 °C for 5 mins and then cooled for 10 mins. After purification, the noble gases (except helium, not measured in this study) were trapped on activated charcoal at 25 K. Subsequently, the cold trap was used to sequentially release Ne, Ar, Kr, and Xe fractions at temperatures of 77, 165, 198, and 335 K, respectively. The released gases were exposed to a final SAES getter for 5 mins before introduction into the Noblesse mass spectrometer (NuInstruments, Ametek) for measurement of elemental abundance and isotope composition. Note that gases were analyzed in the following order: Ne, Kr, Xe, and Ar. The Ar released at 165 K was isolated in a ~1 L stainless steel reservoir during the analysis of Kr and Xe. Aliquots of the air standard were measured regularly to assess the sensitivity and reproducibility of the mass spectrometer and to correct for instrumental fractionation effects. The reported errors on isotopic ratios include the internal error of the measurement, the propagated uncertainty of a series of standard measurements, and uncertainty in the isotopic composition of the instrument blank. Analytical blanks were determined by letting the gas accumulate in the crusher without lifting the ball up and down. Blank quantities, typically 1.6×10^{-17}, 1.1×10^{-15}, 6.7×10^{-18} and 3.4×10^{-19} mol of ^{22}Ne, ^{36}Ar, ^{84}Kr, and ^{130}Xe, respectively, were almost negligible (<5%) compared to quantities of gas released from the samples.

2.6. Ar-Ar measurements

Four quartz samples and one agate sample from the Rochechouart impact structure were analyzed for irradiation-produced and naturally occurring isotopes of Ar, Kr, and Xe by combined in vacuo crushing and stepwise heating at the University of Queensland (UQ).

The high purity mineral separates were washed in distilled water and ethanol and packed into Al-foil sample packets. The sample packets were loaded together with irradiation standards (Hb3Gr, CaF_2, KSO_4, scapolites SY BB1 and BB2) in a silica glass canister and irradiated for 44 hours in the central position of the McClellan Research and Reactor Centre, UC Davis (11 January 2021; RS#7). After return to the noble gas lab ~100 mg sized aliquots of each sample were unpacked and loaded into modified Nupro® valves for in vacuo crushing to preferentially release gases trapped in fluid inclusions. The samples were baked at ~140 °C for 36 hours to achieve ultra-high vacuum in the Nupro® valve crushers and sequentially analyzed in 2-3 crushing steps. The extracted noble gases were purified using three SAES getters over a period of 20 minutes and expanded into the MAP 215-50 noble gas mass spectrometer.

The crushed sample residues were unloaded, packed in Sn-foil capsules, and then reloaded into an ultrahigh vacuum sample holder. The samples were re-baked at ~140 °C for 36 hours to achieve ultra-high vacuum. Individual samples were then dropped into the crucible of a UHV resistance furnace and gases were extracted in 20 min heating steps at temperatures of 400, 700, 1000 or 1100, and 1500 °C. To ensure complete outgassing of the samples each sample was heated in two 1500 °C steps. The extracted noble gases were purified using SAES getters over a period of 20 minutes and expanded into the MAP 215-50 noble gas mass spectrometer.

The isotopes of Ar, Kr, and Xe were measured in peak jumping mode in 7 cycles over a period of 50 minutes. The isotopes of Ar were measured on a Faraday collector and the less abundant isotopes of Kr and Xe were measured on a Balzers electron multiplier. Standard corrections were made for mass discrimination based on the atmospheric $^{40}Ar/^{36}Ar$ ratio of 298.6 (Lee et al., 2006) monitored with daily air calibrations, Ar-isotope interference reactions and radioactive decay of ^{37}Ar (see Kendrick, 2012 for details). Production of $^{39}Ar_K$, $^{38}Ar_{Cl}$, $^{37}Ar_{Ca}$, $^{80}Kr_{Br}$, and $^{128}Xe_I$ from the parent elements K, Cl, Ca, Br, and I was monitored using Hb3Gr and scapolite standards (Kendrick et al., 2013) and CaF_2 and KSO_4 were used to monitor Ar-interference reactions. The samples received a total neutron flux of 3.3×10^{18} neutrons cm^{-2} with a fast/thermal ratio of 1.02 (J value = 0.00869). Production ratios of irradiation produced noble gas isotopes was similar to previous irradiations at the McClellan Research and Reactor Center at the 1-4% level. Chlorine and Br abundances determined from irradiation-produced noble gas isotopes have a repeatability between different irradiations of ~5%, while I/Cl has a repeatability of ~10% (2σ) limited by the homogeneity of the scapolite standard (Kendrick, 2012; Kendrick et al., 2013). The reported uncertainty in the initial $^{40}Ar/^{36}Ar$ isotope measurements includes uncertainty in the correction for radiogenic ^{40}Ar and varied from 0.6% (2σ) to much higher values depending on the amount of gas available for analysis.

3. Results

Abundances and isotope ratios of noble gases measured on non-irradiated samples are reported in Table S1 (Supplementary Material) and results for irradiated samples are reported in Table S2 (Supplementary Material).

3.1. Elemental abundances for non-irradiated samples

Noble gas elemental abundances in the mineral hosts released during all crushing steps range from $5.2x10^{-18}$ to $1.7x10^{-14}$ mol/g for ^{22}Ne, from $3.2x10^{-14}$ to $6.0x10^{-13}$ mol/g for ^{36}Ar, from $4.2x10^{-16}$ to $9.0x10^{-15}$ mol/g for ^{84}Kr, and from $2.5x10^{-18}$ to $5.6x10^{-17}$ mol/g for ^{130}Xe. These abundances are at the lower end of the range of noble gas abundances measured in sedimentary rocks and minerals (Matsubara et al., 1991). Elemental abundance ratios for each sample are compared to noble gas abundance ratios in air, in air-saturated water, in seawater, and in brines in Fig. 3 (Kendrick and Burnard, 2013). Overall, elemental ratios of noble gases are close to those of ambient air and do not show the enrichment in heavy noble gases relative to light ones often measured for noble gases dissolved in water. Sample ROC-AGATA4 displays a clear depletion of neon, by almost two orders of magnitude, compared to air.

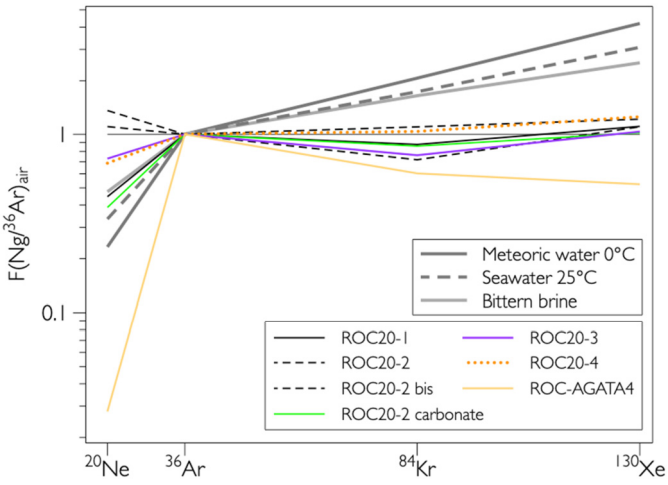

Fig. 3. Elemental abundances of noble gases released from fluid inclusions contained in non-irradiated samples from Rochechouart. Abundances are expressed with the F value. For example, $F(^{20}Ne/^{36}Ar)_{air} = (^{20}Ne/^{36}Ar)_{sample}/(^{20}Ne/^{36}Ar)_{air}$. Only results for non-irradiated samples are shown. Typical errors for elemental ratios are < 30% (2σ). Elemental fractionation patterns for noble gases dissolved in meteoric water (0 °C), seawater (25 °C), and bittern brine (evaporated seawater) are shown for comparison (Kendrick and Burnard, 2013 and refs. therein).

3.2. Isotope ratios for non-irradiated samples

$^{20}Ne/^{22}Ne$ and $^{21}Ne/^{22}Ne$ ratios range from 8.6 to 9.9 and from 0.028 to 0.040, respectively. Most datapoints cluster around the isotopic composition of modern atmospheric neon ($^{20}Ne/^{22}Ne$=9.8 and $^{21}Ne/^{22}Ne$=0.029) (Ozima and Podosek, 2002) (Fig. 4). Neon released by crushing steps on two samples plot far off from the atmospheric value. Neon isotope ratios in the two first crushing steps of the agate sample ROC-AGATA4 are lower than Air and plot close to the mass-dependent fractionation ($m^{1/2}$) curve passing through modern atmospheric neon. This anomalous and seemingly fractionated component is released from the agate sample. Neon in the three first crushing steps of sample ROC20-2bis has elevated $^{21}Ne/^{22}Ne$ ratios and plot slightly above the "Crustal line" of Kennedy et al. (1990) based on gases in sedimentary basins and below the line typical of older basement rocks (Lippmann-Pipke et al., 2011; Kendrick et al., 2011a,b; Holland et al., 2013).

$^{40}Ar/^{36}Ar$ and $^{38}Ar/^{36}Ar$ ratios of the non-irradiated samples range from 298 to 314 and from 0.186 to 0.191, respectively (Fig. 5). Note that the analyses of Ar isotopes in extraction steps #1 and 4 of sample ROC20-2 and #1 of sample ROC20-3 were compromised and corresponding data are therefore not reported in Table S1 nor in Fig. 5. $^{38}Ar/^{36}Ar$ ratios are identical within errors to the isotope composition of atmospheric argon with a weighted mean of 0.18839±0.00043 (MSWD=1.78, $p(\chi^2)$=0.0052, computed with the Isoplot software, Ludwig, 1991). The average $^{40}Ar/^{36}Ar$ ratio for all samples and for all crushing steps is 304.9±6.8 (2σ), about 2% higher than the modern value of 298.56±0.6 (2σ) for atmospheric argon (Lee et al., 2006).

Isotope ratios of krypton (Fig. 6a) and xenon (Fig. 6b) are identical within uncertainty to the isotopic composition of modern Air.

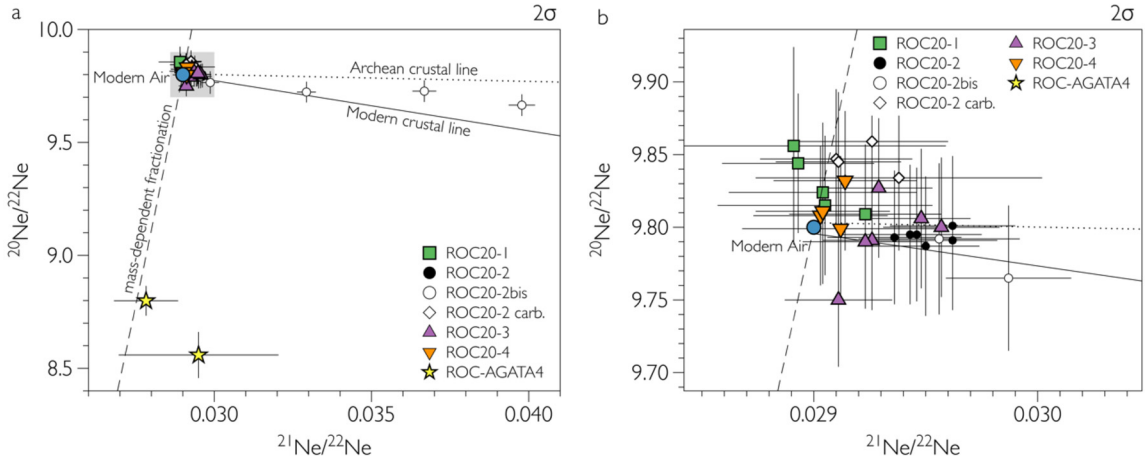

Fig. 4. Three isotope diagrams of neon isotopes measured in non-irradiated samples from Rochechouart. (a) Isotope ratios of neon of gas contained in fluid inclusions of Rochechouart samples analyzed in this study. "Air" corresponds to the isotopic composition of modern atmospheric neon. The gray area illustrates the magnification area in (b). The "Modern crustal" and "Archean crustal" lines depict addition of nucleogenic ^{21}Ne and ^{22}Ne to a starting atmospheric composition. The "Modern crustal" line (plain line) is the one defined by Kennedy et al. (1990), the "Archean crustal line" (dotted line) corresponds to the line defined by Holland et al. (2013). The dashed line corresponds to the mass-dependent fractionation of atmospheric neon with a $m^{1/2}$ dependency. (b) Close-up view of the area close to Air. Lines are the same as in (a). Errors are at 2σ.

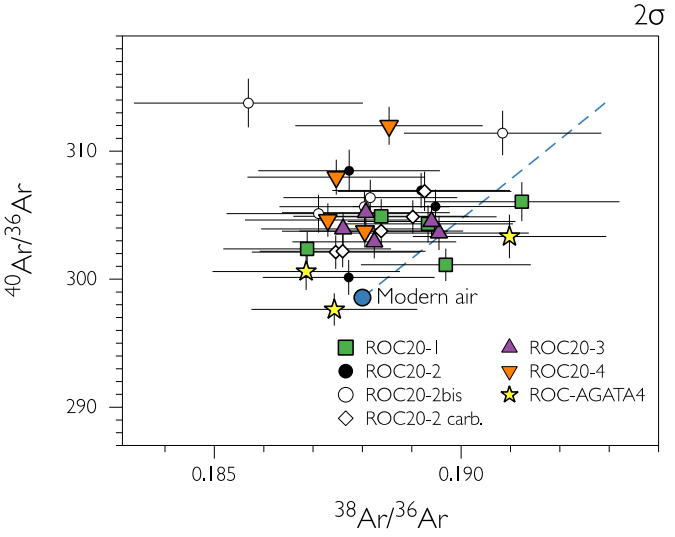

Fig. 5. Three-isotope diagram of argon isotopes of gas contained in fluid inclusions of Rochechouart samples. The dashed line corresponds to the mass-dependent fractionation line (with $m^{1/2}$ relationship) passing through the isotopic composition of modern Air (Ozima and Podosek, 2002). Error bars for non-irradiated samples are at 2σ.

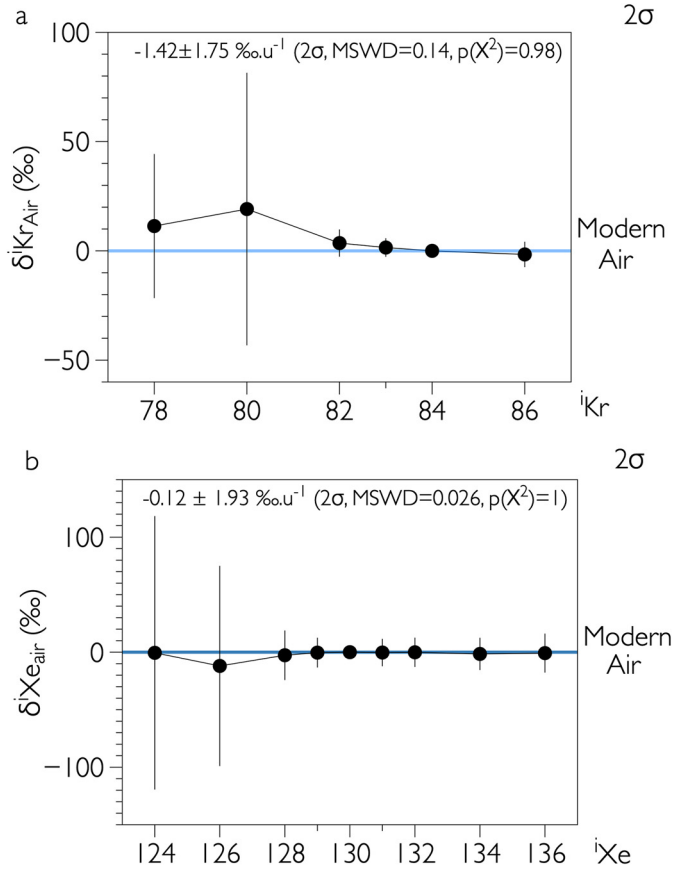

Fig. 6. Isotopic spectra of krypton and xenon released from fluid inclusions of Rochechouart samples (average and standard deviation of total gas released from all samples). (a) Isotope ratios of krypton are expressed using the delta notation ($\delta^{i}Kr_{air} = (({}^{i}Kr/{}^{84}Kr)_{Rochechouart}/({}^{i}Kr/{}^{84}Kr)_{Air})\times 1000$). (b) Isotope ratios of xenon are expressed using the delta notation ($\delta^{i}Xe_{air} = (({}^{i}Xe/{}^{130}Xe)_{Rochechouart}/({}^{i}Xe/{}^{130}Xe)_{Air})\times 1000$). No isotopic fractionation was detected (0.10±0.83‰.u^{-1}, computed with the Isoplot software). Error bars for non-irradiated samples are at 2σ.

3.3. Ar-Ar results

The irradiated sample aliquots were crushed two to three times depending on the amount of gas released in the previous crushing step. Previous work has shown that fluids are expelled from quartz at temperature intervals of 200-700 °C (decrepitation of fluid inclusions) and 1200-1500 °C (expulsion of structural water) (Kendrick and Burnard, 2013). Sample ROC20-4 Ar-Ar was analyzed in five heating steps (400, 700, 1000, 1500, and again at 1500 °C) but because of the relatively small amounts of gas, subsequent samples were analyzed in four heating steps starting at 700 °C (Table S2).

In vacuo crushing extracted noble gases from fluid inclusions with low $K/^{36}Ar$ and typical measured $^{40}Ar/^{36}Ar$ ratios of ~296 to ~310 (Table S2). These values are similar to those obtained on non-irradiated samples. In contrast, step heating of the crushed sample residues, which releases noble gases from both remaining fluid inclusions and very minor K-bearing impurities in the samples, gives higher $K/^{36}Ar$ and $^{40}Ar/^{36}Ar$ ratios (Table S2). The measured $^{40}Ar/^{36}Ar$ ratio in each extraction step is broadly correlated with $K/^{36}Ar$ demonstrating that a significant portion of the ^{40}Ar released from the samples is radiogenic ^{40}Ar produced from in situ radioactive decay of ^{40}K within the ~200 Ma samples.

The initial $^{40}Ar/^{36}Ar$ ratios ($^{40}Ar_{initial}/^{36}Ar$) correspond to $^{40}Ar/^{36}Ar$ ratios corrected for post-entrapment production of radio-

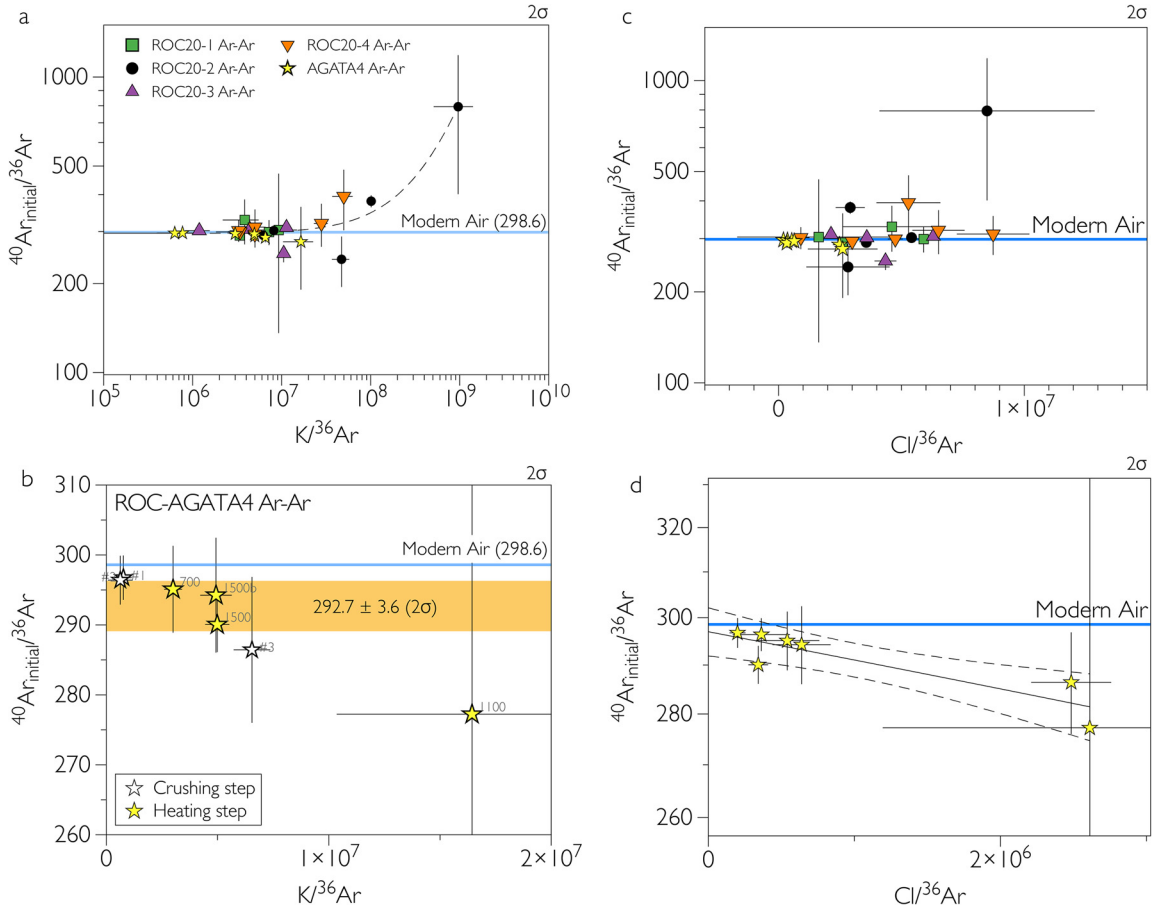

Fig. 7. Results of Ar-Ar measurements. Argon isotopes have been released from Rochechouart samples by vacuo crushing and stepwise heating. K and Cl are calculated from irradiation-produced ^{39}Ar and ^{38}Ar, respectively. The $^{40}Ar_{initial}/^{36}Ar$ ratios correspond to the $^{40}Ar/^{36}Ar$ ratios corrected for in-situ decay of ^{40} K during ~200 Ma. (a) $^{40}Ar_{initial}/^{36}Ar$ vs. $K/^{36}Ar$ space. Most samples show only minimal amounts of parentless radiogenic ^{40}Ar and have air-like $^{40}Ar_{initial}/^{36}Ar$ ratios. The dashed curve corresponds to a linear mixing line through the data points and is displayed for illustration. (b) Close-up view of panel (a) for sample ROC-AGATA4. The data define a mixing relationship between an ancient atmospheric end-member with a low $^{40}Ar/^{36}Ar$ ratio and a modern atmospheric end-member ($^{40}Ar/^{36}Ar$=298.6). The weighted mean for this sample is 292.7 ± 3.6 (2σ), which is lower than the modern air value at the 95% confidence level. (c) $^{40}Ar_{initial}/^{36}Ar$ vs. $Cl/^{36}Ar$ space. Most samples have variable $Cl/^{36}Ar$ and $^{40}Ar/^{36}Ar$ ratios slightly greater than 298.6. The distribution of data might reflect mixing of modern Air and ancient fluids, but Cl-rich fluids contain some parentless excess ^{40}Ar. (d) Close-up view of the $^{40}Ar_{initial}/^{36}Ar$ vs. $Cl/^{36}Ar$ space for the ROC-AGATA4 Ar-Ar sample. This sample contains two clearly distinct components including modern Air and an ancient air-saturated saline fluid with low $^{40}Ar/^{36}Ar$ ratio. Errors are at 2σ.

genic $^{40}Ar^*$, based on an age of 206.9 Ma (Cohen et al., 2017) and the K measured within each sample (Fig. 7). The reported uncertainty in the initial $^{40}Ar/^{36}Ar$ isotope ratio of fluid inclusions in the samples includes uncertainty in the correction for radiogenic ^{40}Ar based on the K content measured as $^{39}Ar_K$ and an assumed age of 206.9 Ma. Based on this age, the total uncertainty in the initial $^{40}Ar/^{36}Ar$ isotope is more sensitive to the amount of gas available for analysis than the correction for post-entrapment radiogenic ingrowth. Each sample has one or more extraction step in which the initial $^{40}Ar/^{36}Ar$ ratio is less than the modern atmospheric value of 298.6 (Table S2). The lowest values in ROC20-1ArAr and ROC20-3ArAr were determined for steps with very low gas volumes, meaning they were sensitive to the blank correction, and are considered unreliable. However, every step for the agate sample ROC-AGATA4 ArAr gives an initial $^{40}Ar/^{36}Ar$ ratio lower than the modern air value and the weighted mean for this sample of 292.7 ± 3.6 (2σ) is lower than the modern air value of 298.6 ± 0.6 at the 95% confidence level (Fig. 7b). If the Ar isotopes in this sample were affected by mass dependent fractionation similar to the Ne isotopes (enrichment in the heavy isotopes, see above) the original $^{40}Ar/^{36}Ar$ ratio could have been even lower. The $^{84}Kr/^{36}Ar$ and $^{130}Xe/^{36}Ar$ ratios are close to air values and similar to those reported for non-irradiated samples (Fig. 3).

For halogens, chlorine (Cl) was preferentially released from all the samples by in vacuo crushing (Fig. 7c). However, very little Cl was released by crushing sample ROC-AGATA4-ArAr with the sub-atmospheric $^{40}Ar/^{36}Ar$ ratio. The $Cl/^{36}Ar$ and $^{40}Ar/^{36}Ar$ ratios of this sample are negatively correlated (Fig. 7d), which could be explained if the sample contains two distinct components including modern Air and an ancient air-saturated saline fluid with low $^{40}Ar/^{36}Ar$ ratio. The other samples have variable $Cl/^{36}Ar$ and $^{40}Ar/^{36}Ar$ ratios slightly greater than Air (Fig. 7c). The distribution of data in Fig. 7c might again reflect mixing of modern Air and ancient fluids, but in these cases the more Cl-rich fluids contain some parentless excess ^{40}Ar.

Individual extraction steps for every sample have variable Br/Cl and I/Cl ratios, which are subject to substantial uncertainties because of the small amounts of halogen-derived noble gases extracted from the samples. However, the weighted average Br/Cl and I/Cl for each sample (Fig. 8) lies in the range typical of sedimentary formation waters. Each sample has I/Cl ratio somewhat higher than seawater suggesting fluid interaction with organic-rich materials that are rich in iodine (Kendrick and Burnard, 2013). The Br/Cl ratios vary from values typical of evaporated seawater to a distinctly low value in sample ROC-AGATA4-ArAr with the sub-atmospheric $^{40}Ar/^{36}Ar$ that might be attributed to dissolution of minor halite

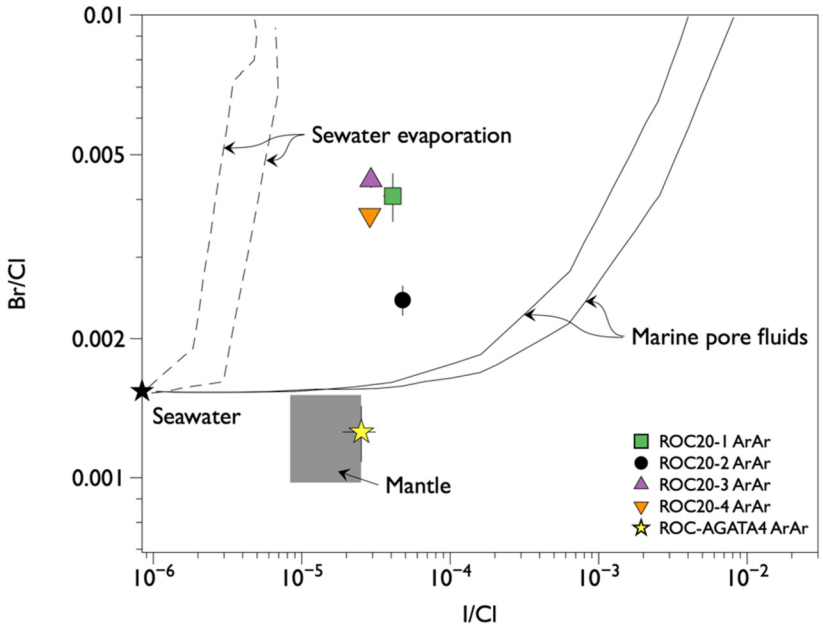

Fig. 8. Total Br/Cl vs. I/Cl ratios obtained on irradiated samples from Rochechouart. The plain lines define the area of data obtained for marine pore fluids enriched with organic Br and I and the dashed lines represent possible seawater evaporation trajectories based on evaporated Black Sea water and Lake Sasyk-Sivash Brines (Kendrick, 2018; Zherebtsova and Volkova, 1966). The grey range is an estimate for the halogen ratios of the mantle based on MORB and OIB glasses (Kendrick et al., 2017). Compositions (except for the ROC-AGATA4 sample) are similar to Mid Continent MVT fluids (Kendrick and Burnard, 2013; Richard et al., 2014) reflecting typical composition of sedimentary formation waters. Error bars at 2σ.

and highlights the distinctly different origin of the fluids trapped in this sample with low $^{40}Ar/^{36}Ar$ compared to the other samples.

4. Discussion

4.1. Incorporation of paleo-atmospheric noble gases

The detection of paleo-atmospheric argon with $^{40}Ar/^{36}Ar$ of less than the modern air value provides strong evidence that the Rochechouart minerals trap a well-preserved paleo-atmospheric signal (Fig. 7). This is further supported by the isotopic compositions of Kr and Xe in all the samples that are within uncertainty of the atmospheric values which are expected to have been constant for the last 200 Ma, although some degree of contamination by modern atmospheric noble gases cannot be fully excluded (Fig. 6). The fact that none of these ratios are mass fractionated provides evidence against significant post-entrapment leakage of noble gases heavier than neon from the fluid inclusions. One sample contains nucleogenic neon isotopes (ROC20-2 bis) and one sample (ROC-AGATA4) shows partial leakage of neon (Fig. 4) with unusually low abundance of neon (Fig. 3) and fractionated isotopic ratios for this element (see below). These two observations highlight the persisting difficulties for identifying clean paleo-atmospheric neon signals although most samples have air-like neon isotopic ratios.

The prevalence of atmospheric noble gases measured in this study, accompanied by very minor contamination with radiogenic ^{40}Ar or nucleogenic ^{21}Ne, suggests the fluid inclusions are dominated by surface-derived waters that were either present as pore fluids in the country rocks or overlay the impact site at the time of the impact (Lambert, 2010 and refs. therein).

However, elemental ratios of noble gases in fluids released from fluid inclusions do not show the fractionation in favor of heavy noble gases usually measured for noble gases dissolved in water, seawater or for noble gases trapped in sediments (Fig. 3, Podosek et al., 1980). Preferential release of light relative to heavy noble gases originally trapped in sediments (Kendrick et al., 2011b) or elemental fractionation by various processes (phase separation during boiling, interaction with sediments etc., see Kendrick and Burnard, 2013) during the fluid's journey in Earth's crust could be responsible for mimicking an air-like pattern. Note that recent results obtained on Archean hydrothermal quartz crystals containing fractionated paleo-atmospheric xenon (Avice et al., 2017) reveal that noble gases trapped in fluid inclusions of those samples seem to preserve the elevated Xe/Kr ratio expected for the Archean atmosphere (Broadley et al., 2022).

4.2. Crustal contributions and post-entrapment modifications

While most measurements reveal an almost pure atmospheric signature, some crushing steps show deviations relative to the elemental and isotopic composition of atmospheric noble gases. For example, two samples show neon isotopic ratios significantly different from the composition of modern Air (Fig. 4). Results obtained for sample ROC20-2bis plot in-between the 'modern line' typical of sedimentary basins and a crustal line previously reported for fluids or fluid inclusions in Proterozoic and Archean basement lithologies. The high $^{21}Ne/^{22}Ne$ ratio together with air-like $^{20}Ne/^{22}Ne$ suggests production of nucleogenic neon from U-minerals with a higher O/F ratio than is typical of sedimentary basins (Holland et al., 2013; Kendrick et al., 2011a; Kennedy et al., 1990; Lippmann-Pipke et al., 2011). Note that analysis of another split from the same sample (ROC20-2) did not reveal any nucleogenic contribution implying that the nucleogenic component is heterogeneously dispersed through the sample and not contained in all fluid inclusions. Furthermore, the nucleogenic contribution is much less pronounced than for crustal fluids sampled in other studies since the $^{21}Ne/^{22}Ne$ ratio for Rochechouart samples reaches a maximum value of 0.03978 ± 0.00042 (2σ), relatively close to the atmospheric ratio of 0.029 (Ozima and Podosek, 2002) while neon released from fluid inclusions contained in samples from the Kaapvaal craton show $^{21}Ne/^{22}Ne$ ratio up to 0.585 ± 0.08 (2σ), for example (Lippmann-Pipke et al., 2011). The facts that the nucleogenic contribution is small, detected for only one sample and not in the duplicated measurements suggest that production of nucleogenic neon remained limited in the Rochechouart area or at least

that the nucleogenic signal has been strongly diluted by surface-derived fluids with an air-like isotopic composition of neon.

The elemental and isotopic compositions of neon released from the agate sample ROC-AGATA4 are clearly distinct from those of atmospheric Ne. Neon is selectively depleted in this sample as evidenced by a low Ne/Ar ratio (and Kr/Ar and Xe/Ar ratios closer to Air, Fig. 3). The $^{20}Ne/^{22}Ne$ and $^{21}Ne/^{22}Ne$ ratios are also low and plot along the mass-dependent fractionation line (Fig. 4). One possibility is that part of neon originally present in this sample escaped. The remaining fraction became enriched in heavy isotopes. The fact that only neon, and not heavier noble gases, is concerned suggests that neon atoms were small enough to diffuse out from microcrystalline quartz while heavier and bigger noble gas atoms (Ar, Kr, and Xe) stayed trapped within the minerals.

4.3. Paleo-atmospheric $^{40}Ar/^{36}Ar$ ratio

Ar-Ar results obtained on the agate sample confirm that 200 Ma-ago, atmospheric argon had a $^{40}Ar/^{36}Ar$ ratio of 292.7±3.6 (2σ) or lower (Fig. 7). This result is coherent with the possibly slightly lower atmospheric $^{40}Ar/^{36}Ar$ ratio reported for the Devonian atmosphere ($^{40}Ar/^{36}Ar$ of 289.5±0.8 (2σ)) (Cadogan, 1977; Stuart et al., 2016) and agrees with most existing models of argon isotope systematics which try to link the mantle, the crust, and the atmosphere and propose different scenarios for the evolution of the atmospheric $^{40}Ar/^{36}Ar$ with time (*e.g.*, Guo and Korenaga, 2020; Pujol et al., 2013; Stuart et al., 2016). Being able to derive this low $^{40}Ar/^{36}Ar$ ratio for the Mesozoic atmosphere demonstrates that Rochechouart samples did trap ancient atmospheric gases but also that the composition of the paleo-atmospheric gases trapped in post-impact hydrothermal minerals is only marginally affected by the presence of parentless radiogenic ^{40}Ar commonly found in hydrothermal quartz from other geological settings (Rama et al., 1965). Post-impact hydrothermal minerals should thus be priority targets for building a detailed curve of the evolution of the atmospheric $^{40}Ar/^{36}Ar$ ratio with time, which could in turn be used to put constraints on Earth's mantle degassing and continental crust growth histories (Avice et al., 2017; Marty et al., 2019; Stuart et al., 2016; Zhang et al., 2023).

4.4. Feasibility for other and older impact structures

Results obtained in the present study reveal for the first time that minerals formed in impact-generated hydrothermal systems represent time capsules recording the composition of noble gases in the ancient atmosphere. Impact structures younger than 200 Ma-old should thus be high-priority targets for future paleo-atmospheric studies. Impact structures older than 200 Ma should also be scrutinized cautiously to evaluate if geological events such as regional-scale metamorphism erased the paleo-atmospheric record or introduced a younger atmospheric component. Previous studies of Archean hydrothermal quartz, not related to impacts, demonstrated that paleo-atmospheric gases can be retained in geological samples for billions of years (Avice et al., 2018), suggesting that even the hydrothermal quartz deposited in the oldest impact craters could contain very old paleo-atmospheric components, provided that later post-impact events did not introduce gases of unknown origin trapped in secondary inclusions of unknown age.

Results obtained in the present study suggest that hydrothermal minerals present in impact structures at the surface of other planets of the solar system could also carry important information on the surface conditions of the planet at the time of the impact. A very good example is Mars. The cratering record of Mars covers most of the geological history of the planet, including the first 1 Gyr of evolution when atmospheric evolution was probably the most significant (Cassata et al., 2022). Furthermore, there are growing evidence for the presence of hydrothermal systems in some Martian craters (Osinski et al., 2013). Such hydrothermal systems should be explored by present or future robotic missions and sampled to evaluate if they host traces of past life but also to put constraints on the atmospheric history of Mars. Studies of Martian atmospheric gases trapped in Martian meteorites already suggest that the elemental and isotopic composition of the Martian atmosphere changed with time (Avice and Marty, 2020; Cassata, 2017; Cassata et al., 2022). Returning post-impact hydrothermal minerals from a Martian crater would certainly provide additional constraints on the geological history of Mars, of its atmosphere, and also on the nature of surface fluids, provided that the impact can be dated with relevant accuracy and precision (Farley et al., 2014).

5. Conclusions

Understanding the evolution of the composition of the Earth's atmosphere requires to build a consequent collection of paleo-atmospheric proxies whose study can be compared to modeling efforts. Results obtained in this study demonstrate that post-impact hydrothermal minerals record the composition of the ancient 200 Myr-old atmosphere with only rare and minimal post-entrapment modifications. Post-impact hydrothermal minerals can thus be considered as new paleo-atmospheric proxies. Future work will explore if paleo-signatures can be detected in hydrothermal quartz deposited in much older impact structures (*e.g.*, in the 1.8 Ga old Sudbury impact structure) and if other mineral phases also recorded the composition of the paleo-atmosphere.

CRediT authorship contribution statement

G. Avice: Conceptualization, Data curation, Formal analysis, Funding acquisition, Investigation, Methodology, Supervision, Validation, Writing – original draft, Writing – review & editing. **M.A. Kendrick:** Formal analysis, Investigation, Methodology, Writing – review & editing, Writing – original draft. **A. Richard:** Investigation, Methodology, Validation, Writing – original draft. **L. Ferrière:** Resources, Writing – original draft, Writing – review & editing.

Declaration of competing interest

The authors declare that they have no known competing financial interests or personal relationships that could have appeared to influence the work reported in this paper.

Data availability

Data will be made available on request.

Acknowledgements

G.A. thanks the Institut de physique du globe de Paris (IPGP), the French "Programme National de Planétologie" (PNP) and the Centre National de la Recherche Scientifique (CNRS) for their financial support. L.F. thanks Philippe Chèvremont (France) for the donation of the samples, now part of the impactite collection of the Natural History Museum Vienna (Austria), that were used for this study. This project has received funding from the European Research Council (ERC) under the European Union's Horizon Europe research and innovation program (grant agreement no. 101041122 to G.A.). The authors thank two anonymous reviewers for their constructive comments and R. Dasgupta for his careful editorial handling.

Appendix A. Supplementary material

Supplementary material related to this article can be found online at https://doi.org/10.1016/j.epsl.2023.118351.

References

Abramov, O., 2004. Numerical modeling of an impact-induced hydrothermal system at the Sudbury crater. J. Geophys. Res. 109, 10,083. https://doi.org/10.1029/2003JE002213.

Almayrac, M.G., Broadley, M.W., Bekaert, D.V., Hofmann, A., Marty, B., 2021. Possible discontinuous evolution of atmospheric xenon suggested by Archean barites. Chem. Geol. 581, 120405. https://doi.org/10.1016/j.chemgeo.2021.120405.

Ames, D.E., Watkinson, D.H., Parrish, R.R., 1998. Dating of a regional hydrothermal system induced by the 1850 Ma Sudbury impact event. Geology 26, 447–450. https://doi.org/10.1130/0091-7613(1998)026<0447:DOARHS>2.3.CO;2.

Ardoin, L., Broadley, M.W., Almayrac, M., Avice, G., Byrne, D.J., Tarantola, A., Lepland, A., Saito, T., Komiya, T., Shibuya, T., Marty, B., 2022. The end of the isotopic evolution of atmospheric xenon. Geochem. Perspect. Lett. 20, 43–47. https://doi.org/10.7185/geochemlet.2207.

Avice, G., Marty, B., 2020. Perspectives on atmospheric evolution from noble gas and nitrogen isotopes on Earth, Mars & Venus. Space Sci. Rev. 216, 36. https://doi.org/10.1007/s11214-020-00655-0.

Avice, G., Marty, B., Burgess, R., 2017. The origin and degassing history of the Earth's atmosphere revealed by Archean xenon. Nat. Commun. 8, 15455. https://doi.org/10.1038/ncomms15455.

Avice, G., Marty, B., Burgess, R., Hofmann, A., Philippot, P., Zahnle, K., Zakharov, D., 2018. Evolution of atmospheric xenon and other noble gases inferred from Archean to Paleoproterozoic rocks. Geochim. Cosmochim. Acta 232, 82–100. https://doi.org/10.1016/j.gca.2018.04.018.

Bischoff, L., Oskierski, W., 1987. Fractures, pseudotachylite veins and breccia dikes in the crater floor of the Rochechouart impact structure, SW-France, as indicators of crater forming processes. In: Pohl, J. (Ed.), Research in Terrestrial Impact Structures. Vieweg+Teubner Verlag, Wiesbaden, pp. 5–29.

Bons, P.D., Elburg, M.A., Gomez-Rivas, E., 2012. A review of the formation of tectonic veins and their microstructures. J. Struct. Geol. 43, 33–62. https://doi.org/10.1016/j.jsg.2012.07.005.

Broadley, M.W., Byrne, D.J., Ardoin, L., Almayrac, M.G., Bekaert, D.V., Marty, B., 2022. High precision noble gas measurements of hydrothermal quartz reveal variable loss rate of Xe from the Archean atmosphere. Earth Planet. Sci. Lett. 588, 117577. https://doi.org/10.1016/j.epsl.2022.117577.

Burnard, P. (Ed.), 2013. The Noble Gases as Geochemical Tracers. Springer Berlin Heidelberg, Berlin, Heidelberg.

Cadogan, P.H., 1977. Palaeoatmospheric argon in Rhynie chert. Nature 268, 38–41. https://doi.org/10.1038/268038a0.

Cassata, W.S., 2017. Meteorite constraints on Martian atmospheric loss and paleoclimate. Earth Planet. Sci. Lett. 479, 322–329. https://doi.org/10.1016/j.epsl.2017.09.034.

Cassata, W.S., Zahnle, K.J., Samperton, K.M., Stephenson, P.C., Wimpenny, J., 2022. Xenon isotope constraints on ancient Martian atmospheric escape. Earth Planet. Sci. Lett. 580, 117349. https://doi.org/10.1016/j.epsl.2021.117349.

Catling, D.C., Kasting, J.F., 2017. Atmospheric Evolution on Inhabited and Lifeless Worlds. Cambridge University Press, Cambridge.

Catling, D.C., Zahnle, K.J., 2020. The Archean atmosphere. Sci. Adv. 6, eaax1420. https://doi.org/10.1126/sciadv.aax1420.

Chèvremont, P., Floc'h, J.P., Ménillet, F., Stussi, J.M., Delbos, R., Sauret, B., Blès, J.L., Courbe, C., Vuaillat, D., Gravelat, C., 1996. Notice explicative, Carte Géologique de la France (1/50000), feuille de Rochechouart (687).

Cohen, B.E., Mark, D.F., Lee, M.R., Simpson, S.L., 2017. A new high-precision 40Ar/39Ar age for the Rochechouart impact structure: at least 5 Ma older than the Triassic-Jurassic boundary. Meteorit. Planet. Sci. 52, 1600–1611. https://doi.org/10.1111/maps.12880.

Ehlmann, B.L., Anderson, F.S., Andrews-Hanna, J., Catling, D.C., Christensen, P.R., Cohen, B.A., Dressing, C.D., Edwards, C.S., Elkins-Tanton, L.T., Farley, K.A., Fassett, C.I., Fischer, W.W., Fraeman, A.A., Golombek, M.P., Hamilton, V.E., Hayes, A.G., Herd, C.D.K., Horgan, B., Hu, R., Jakosky, B.M., Johnson, J.R., Kasting, J.F., Kerber, L., Kinch, K.M., Kite, E.S., Knutson, H.A., Lunine, J.I., Mahaffy, P.R., Mangold, N., McCubbin, F.M., Mustard, J.F., Niles, P.B., Quantin-Nataf, C., Rice, M.S., Stack, K.M., Stevenson, D.J., Stewart, S.T., Toplis, M.J., Usui, T., Weiss, B.P., Werner, S.C., Wordsworth, R.D., Wray, J.J., Yingst, R.A., Yung, Y.L., Zahnle, K.J., 2016. The sustainability of habitability on terrestrial planets: insights, questions, and needed measurements from Mars for understanding the evolution of Earth-like worlds. J. Geophys. Res., Planets 121, 1927–1961. https://doi.org/10.1002/2016JE005134.

Farley, K.A., Malespin, C., Mahaffy, P., Grotzinger, J.P., Vasconcelos, P.M., Milliken, R.E., Malin, M., Edgett, K.S., Pavlov, A.A., Hurowitz, J.A., Grant, J.A., Miller, H.B., Arvidson, R., Beegle, L., Calef, F., Conrad, P.G., Dietrich, W.E., Eigenbrode, J., Gellert, R., Gupta, S., Hamilton, V., Hassler, D.M., Lewis, K.W., McLennan, S.M., Ming, D., Navarro-González, R., Schwenzer, S.P., Steele, A., Stolper, E.M., Sumner, D.Y., Vaniman, D., Vasavada, A., Williford, K., Wimmer-Schweingruber, R.F., the MSL Science Team, Blake, D.F., Bristow, T., DesMarais, D., Edwards, L., Haberle, R., Hoehler, T., Hollingsworth, J., Kahre, M., Keely, L., McKay, C., Wilhelm, M.B., Bleacher, L., Brinckerhoff, W., Choi, D., Dworkin, J.P., Floyd, M., Freissinet, C., Garvin, J., Glavin, D., Harpold, D., Martin, D.K., McAdam, A., Raaen, E., Smith, M.D., Stern, J., Tan, F., Trainer, M., Meyer, M., Posner, A., Voytek, M., Anderson, R.C., Aubrey, A., Behar, A., Blaney, D., Brinza, D., Christensen, L., Crisp, J.A., DeFlores, L., Feldman, J., Feldman, S., Flesch, G., Hurowitz, J., Jun, I., Keymeulen, D., Maki, J., Mischna, M., Morookian, J.M., Parker, T., Pavri, B., Schoppers, M., Sengstacken, A., Simmonds, J.J., Spanovich, N., de la T. Juarez, M., Webster, C.R., Yen, A., Archer, P.D., Cucinotta, F., Jones, J.H., Morris, R.V., Niles, P., Rampe, E., Nolan, T., Fisk, M., Radziemski, L., Barraclough, B., Bender, S., Berman, D., Dobrea, E.N., Tokar, R., Williams, R.M.E., Yingst, A., Leshin, L., Cleghorn, T., Huntress, W., Manhès, G., Hudgins, J., Olson, T., Stewart, N., Sarrazin, P., Vicenzi, E., Wilson, S.A., Bullock, M., Ehresmann, B., Peterson, J., Rafkin, S., Zeitlin, C., Fedosov, F., Golovin, D., Karpushkina, N., Kozyrev, A., Litvak, M., Malakhov, A., Mitrofanov, I., Mokrousov, M., Nikiforov, S., Prokhorov, V., Sanin, A., Tretyakov, V., Varenikov, A., Vostrukhin, A., Kuzmin, R., Clark, B., Wolff, M., Botta, O., Drake, D., Bean, K., Lemmon, M., Anderson, R.B., Herkenhoff, K., Lee, E.M., Sucharski, R., de P. Hernández, M.Á., Ávalos, J.J.B., Ramos, M., Kim, M.-H., Plante, I., Muller, J.-P., Ewing, R., Boynton, W., Downs, R., Fitzgibbon, M., Harshman, K., Morrison, S., Kortmann, O., Palucis, M., Williams, A., Lugmair, G., Wilson, M.A., Rubin, D., Jakosky, B., Balic-Zunic, T., Frydenvang, J., Jensen, J.K., Kinch, K., Koefoed, A., Madsen, M.B., Stipp, S.L.S., Boyd, N., Campbell, J.L., Perrett, G., Pradler, I., VanBommel, S., Jacob, S., Owen, T., Rowland, S., Savijärvi, H., Boehm, E., Böttcher, S., Burmeister, S., Guo, J., Köhler, J., García, C.M., Mueller-Mellin, R., Bridges, J.C., McConnochie, T., Benna, M., Franz, H., Bower, H., Brunner, A., Blau, H., Boucher, T., Carmosino, M., Atreya, S., Elliott, H., Halleaux, D., Rennó, N., Wong, M., Pepin, R., Elliott, B., Spray, J., Thompson, L., Gordon, S., Newsom, H., Ollila, A., Williams, J., Bentz, J., Nealson, K., Popa, R., Kah, L.C., Moersch, J., Tate, C., Day, M., Kocurek, G., Hallet, B., Sletten, R., Francis, R., McCullough, E., Cloutis, E., ten Kate, I.L., Kuzmin, R., Fraeman, A., Scholes, D., Slavney, S., Stein, T., Ward, J., Berger, J., Moores, J.E., 2014. In situ radiometric and exposure age dating of the Martian surface. Science 343, 1247166. https://doi.org/10.1126/science.1247166.

Guo, M., Korenaga, J., 2020. Argon constraints on the early growth of felsic continental crust. Sci. Adv. 6, eaaz6234. https://doi.org/10.1126/sciadv.aaz6234.

Gurov, E.P., Koeberl, C., Reimold, W.U., 1998. Petrography and geochemistry of target rocks and impactites from the Ilyinets Crater, Ukraine. Meteorit. Planet. Sci. 33, 1317–1333. https://doi.org/10.1111/j.1945-5100.1998.tb01316.x.

Holland, G., Lollar, B.S., Li, L., Lacrampe-Couloume, G., Slater, G.F., Ballentine, C.J., 2013. Deep fracture fluids isolated in the crust since the Precambrian era. Nature 497, 357–360. https://doi.org/10.1038/nature12127.

Holm-Alwmark, S., Jourdan, F., Ferriere, L., Alwmark, C., Koeberl, C., 2021. Resolving the age of the Puchezh-Katunki impact structure (Russia) against alteration and inherited 40Ar* – No link with extinctions. Geochim. Cosmochim. Acta 301, 116–140. https://doi.org/10.1016/j.gca.2021.03.001.

Jourdan, F., Reimold, W.U., Deutsch, A., 2012. Dating terrestrial impact structures. Elements 8, 49–53. https://doi.org/10.2113/gselements.8.1.49.

Kendrick, M.A., 2018. Halogens in seawater, marine sediments and the altered oceanic lithosphere. In: Harlov, D.E., Aranovich, L. (Eds.), The Role of Halogens in Terrestrial and Extraterrestrial Geochemical Processes, Springer Geochemistry. Springer International Publishing, Cham, pp. 591–648.

Kendrick, M.A., 2012. High precision Cl, Br and I determinations in mineral standards using the noble gas method. Chem. Geol. 292–293, 116–126. https://doi.org/10.1016/j.chemgeo.2011.11.021.

Kendrick, M.A., Arculus, R., Burnard, P., Honda, M., 2013. Quantifying brine assimilation by submarine magmas: examples from the Galápagos Spreading Centre and Lau Basin. Geochim. Cosmochim. Acta 123, 150–165. https://doi.org/10.1016/j.gca.2013.09.012.

Kendrick, M.A., Burnard, P., 2013. Noble gases and halogens in fluid inclusions: a journey through the Earth's crust. In: Burnard, P. (Ed.), The Noble Gases as Geochemical Tracers. Springer, Berlin Heidelberg, Berlin, Heidelberg, pp. 319–369.

Kendrick, M.A., Hémond, C., Kamenetsky, V.S., Danyushevsky, L., Devey, C.W., Rodemann, T., Jackson, M.G., Perfit, M.R., 2017. Seawater cycled throughout Earth's mantle in partially serpentinized lithosphere. Nat. Geosci. 10, 222–228. https://doi.org/10.1038/ngeo2902.

Kendrick, M.A., Honda, M., Oliver, N.H.S., Phillips, D., 2011a. The noble gas systematics of late-orogenic H2O–CO2 fluids, Mt Isa, Australia. Geochim. Cosmochim. Acta 75, 1428–1450. https://doi.org/10.1016/j.gca.2010.12.005.

Kendrick, M.A., Phillips, D., Wallace, M., Miller, J.M., 2011b. Halogens and noble gases in sedimentary formation waters and Zn-Pb deposits: a case study from the Lennard Shelf, Australia. Appl. Geochem. 26, 2089–2100. https://doi.org/10.1016/j.apgeochem.2011.07.007.

Kennedy, B.M., Hiyagon, H., Reynolds, J.H., 1990. Crustal neon: a striking uniformity. Earth Planet. Sci. Lett. 98, 277–286.

Kinnunen, K.A., Lindqvist, K., 1998. Agate as an indicator of impact structures: an example from Sääksjärvi, Finland. Meteorit. Planet. Sci. 33, 7–12. https://doi.org/10.1111/j.1945-5100.1998.tb01603.x.

Kraut, F., 1969. Sur la présence de cônes de pression ('shatter cones') dans les brèches et roches éruptives de la région de Rochechouart. CRH Acad. Sci., Ser. D 269, 1486.

Kraut, F., French, B.M., 1971. The Rochechouart meteorite impact structure, France: preliminary geological results. J. Geophys. Res. 76, 5407–5413. https://doi.org/10.1029/JB076i023p05407.

Lambert, P., 2010. Target and impact deposits at Rochechouart impact structure, France. In: Gibson, R.L., Reimold, W.U. (Eds.), Large Meteorite Impacts and Planetary Evolution IV. In: Geological Society of America Special Paper 465, pp. 509–541.

Lee, J.-Y., Marti, K., Severinghaus, J.P., Kawamura, K., Yoo, H.-S., Lee, J.B., Kim, J.S., 2006. A redetermination of the isotopic abundances of atmospheric Ar. Geochim. Cosmochim. Acta 70, 4507–4512. https://doi.org/10.1016/j.gca.2006.06.1563.

Lippmann-Pipke, J., Lollar, B.S., Niedermann, S., Stroncik, N.A., Naumann, R., van Heerden, E., Onstott, T.C., 2011. Neon identifies two billion year old fluid component in Kaapvaal Craton. Chem. Geol. 283, 287–296. https://doi.org/10.1016/j.chemgeo.2011.01.028.

Ludwig, K.R., 1991. ISOPLOT; a plotting and regression program for radiogenic-isotope data; version 2.53. Open-File Report VL - USGS 91–445, 39.

Marty, B., 2020. Origins and early evolution of the atmosphere and the oceans. Geochem. Perspect. 9, 135–313. https://doi.org/10.7185/geochempersp.9.2.

Marty, B., Bekaert, D.V., Broadley, M.W., Jaupart, C., 2019. Geochemical evidence for high volatile fluxes from the mantle at the end of the Archaean. Nature 575, 485–488. https://doi.org/10.1038/s41586-019-1745-7.

Marty, B., Zimmermann, L., Pujol, M., Burgess, R., Philippot, P., 2013. Nitrogen isotopic composition and density of the Archean atmosphere. Science 342, 101–104. https://doi.org/10.1126/science.1240971.

Matsubara, K., Matsuda, J., Sugisaki, R., 1991. Noble gases in Mesozoic cherts from the U.S.A. and Japan. Chem. Geol., Isot. Geosci. Sect. 86, 287–293. https://doi.org/10.1016/0168-9622(91)90011-K.

Naumov, M.V., 2002. Impact-generated hydrothermal systems: data from Popigai, Kara, and Puchezh-Katunki impact structures. In: Impacts in Precambrian Shields. Impact Studies. Springer, Berlin, Heidelberg.

Osinski, G.R., Grieve, R.A.F., Ferrière, L., Losiak, A., Pickersgill, A.E., Cavosie, A.J., Hibbard, S.M., Hill, P.J.A., Bermudez, J.J., Marion, C.L., Newman, J.D., 2022. Impact Earth: a review of the terrestrial impact record. Earth-Sci. Rev. 232, 104112. https://doi.org/10.1016/j.earscirev.2022.104112.

Osinski, G.R., Tornabene, L.L., Banerjee, N.R., Cockell, C.S., Flemming, R., Izawa, M.R.M., McCutcheon, J., Parnell, J., Preston, L.J., Pickersgill, A.E., Pontefract, A., Sapers, H.M., Southam, G., 2013. Impact-generated hydrothermal systems on Earth and Mars. Icarus 224, 347–363. https://doi.org/10.1016/j.icarus.2012.08.030.

Ozima, M., Podosek, F.A., 2002. Noble Gas Geochemistry, second edition. Cambridge University Press, Cambridge.

Passchier, C.W., Trouw, R.A.J., 2005. Microtectonics. Springer-Verlag, Berlin/Heidelberg.

Podosek, F.A., Honda, M., Ozima, M., 1980. Sedimentary noble gases. Geochim. Cosmochim. Acta 44, 1875–1884. https://doi.org/10.1016/0016-7037(80)90236-7.

Pujol, M., Marty, B., Burgess, R., Turner, G., Philippot, P., 2013. Argon isotopic composition of Archaean atmosphere probes early Earth geodynamics. Nature 498, 87–90. https://doi.org/10.1038/nature12152.

Rama, S.N.I., Hart, S.R., Roedder, E., 1965. Excess radiogenic argon in fluid inclusions. J. Geophys. Res. 70, 509–511. https://doi.org/10.1029/JZ070i002p00509.

Richard, A., Kendrick, M.A., Cathelineau, M., 2014. Noble gases (Ar, Kr, Xe) and halogens (Cl, Br, I) in fluid inclusions from the Athabasca Basin (Canada): Implications for unconformity-related U deposits. Precambrian Res. 247, 110–125. https://doi.org/10.1016/j.precamres.2014.03.020.

Sapers, H.M., Osinski, G.R., Banerjee, N.R., Ferrière, L., Lambert, P., Izawa, M.R.M., 2014. Revisiting the Rochechouart impact structure, France. Meteorit. Planet. Sci. 49, 2152–2168. https://doi.org/10.1111/maps.12381.

Schmieder, M., Buchner, E., Schwarz, W.H., Trieloff, M., Lambert, P., 2010. A Rhaetian 40Ar/39Ar age for the Rochechouart impact structure (France) and implications for the latest Triassic sedimentary record: a Rhaetian age for the Rochechouart impact structure. Meteorit. Planet. Sci. 45, 1225–1242. https://doi.org/10.1111/j.1945-5100.2010.01070.x.

Schmieder, M., Kring, D.A., 2020. Earth's impact events through geologic time: a list of recommended ages for terrestrial impact structures and deposits. Astrobiology 20, ast.2019.2085. https://doi.org/10.1089/ast.2019.2085.

Stuart, F.M., Mark, D.F., Gandanger, P., McConville, P., 2016. Earth-atmosphere evolution based on new determination of Devonian atmosphere Ar isotopic composition. Earth Planet. Sci. Lett. 446, 21–26. https://doi.org/10.1016/j.epsl.2016.04.012.

Turner, G., 1988. Hydrothermal fluids and argon isotopes in quartz veins and cherts. Geochim. Cosmochim. Acta 52, 1443–1448. https://doi.org/10.1016/0016-7037(88)90214-1.

Turpin, L., Cuney, M., Friedrich, M., Bouchez, J.-L., Aubertin, M., 1990. Meta-igneous origin of Hercynian peraluminous granites in N.W. French Massif Central: implications for crustal history reconstructions. Contrib. Mineral. Petrol. 104, 163–172. https://doi.org/10.1007/BF00306440.

Van den Kerkhof, A.M., Hein, U.F., 2001. Fluid inclusion petrography. Lithos 55, 27–47. https://doi.org/10.1016/S0024-4937(00)00037-2.

Wilkinson, J.J., 2001. Fluid inclusions in hydrothermal ore deposits. Lithos 55, 229–272. https://doi.org/10.1016/S0024-4937(00)00047-5.

Zhang, X.J., Avice, G., Parai, R., 2023. Noble gas insights into early impact delivery and volcanic outgassing to Earth's atmosphere: a limited role for the continental crust. Earth Planet. Sci. Lett. 609, 118083. https://doi.org/10.1016/j.epsl.2023.118083.

Zherebtsova, I.K., Volkova, N.N., 1966. Experimental study of behavior of trace elements in the process of natural solar evaporation of Black Sea water and Sasyk-Sivash brine. Geochem. Int. 3, 656–670.